Donor and acceptor concentration dependence of the electron Hall mobility and the Hall scattering factor in *n*-type 4H– and 6H–SiC

Hisaomi Iwata[a] and Kohei M. Itoh[b]
Department of Applied Physics and Physico-Informatics, Keio University, Yokohama 223-8522, Japan

(Received 27 October 2000; accepted for publication 21 February 2001)

Theoretical calculation of the electron Hall mobility and the Hall scattering factor in 4H– and 6H–SiC is performed based on the low-field transport model. Our mobility calculation as a function of temperature, net-doping concentration ($[N_D]$-$[N_A]$), and compensation ratio ($[N_A]/[N_D]$), where N_D and N_A are the donor (nitrogen) and acceptor concentrations, respectively, provides the theoretical values of the electron Hall mobility expected for the high quality SiC crystal. The results can be used for the evaluation of the crystalline quality of a given SiC sample. We also present the ratio of the Hall and drift mobility, i.e., the Hall scattering factor, which is needed to make a bridge between the experimentally measured Hall mobility and the theoretically calculated drift mobility using, for example, Monte Carlo simulation. Our calculations of both the electron Hall mobility and the Hall scattering factor are in very good agreement with the experimental results. © *2001 American Institute of Physics.* [DOI: 10.1063/1.1366660]

I. INTRODUCTION

The worldwide interest in silicon carbide for electronic device applications is now greater than ever because of the recent progress in the crystal growth technology. Two of the most popular polytypes, 4H– and 6H–SiC, have been studied intensively in the past decades due to their excellent properties such as high electric break down field, high thermal conductivity, and large saturation electron drift velocity. These properties lead to much better device performance than silicon for high-voltage power applications and for high-temperature operations.[1,2]

In contrast to the recent intensive growth and characterization studies on 4H– and 6H–SiC, theoretical studies on electron transport have been rather limited.[3–13] Except for Ref. 13 that has treated the transport properties of 4H–SiC taking into account the effect of the externally applied magnetic field, most of the transport studies have been based on Monte Carlo simulation in which the effect of the externally applied magnetic field cannot be included, i.e., they have provided the drift mobility. On the other hand, the Hall mobility, which is obtained from the Hall effect measurement, is the one most often determined experimentally. Thus, quantitative knowledge of the ratio of the electron Hall and drift mobility, i.e., the Hall scattering factor, is necessary to compare experimental results with Monte Carlo calculation directly.[3–7] The key for understanding of the electron transport in 4H– and 6H–SiC is their strong anisotropy of the conduction band structure. The electron Hall mobility in 4H– and 6H–SiC are described by a strong function of the directions of the externally applied electric and magnetic field.[11–13] The Hall scattering factor is also affected by the anisotropy in the electron effective mass tensors. In order to provide a prescription to the problem of the anisotropy of the electron Hall mobility in 4H– and 6H–SiC, we have recently reported the theory in which we present analytical expressions for the electron Hall mobility in the three distinct Hall measurement configurations as shown in Figs. 1(a) [$\mathbf{B}\|\mathbf{c}$, $\mathbf{j}\perp\mathbf{c}$], 1(b) [$\mathbf{B}\perp\mathbf{c}$, $\mathbf{j}\perp\mathbf{c}$], and 1(c) [$\mathbf{B}\perp\mathbf{c}$, $\mathbf{j}\|\mathbf{c}$], where **B**, **j**, and **c** are the directions of the magnetic field, current flow, and *c* axis of the hexagonal unit cell, respectively.[11] In Ref. 11, we have demonstrated that the strong anisotropy of the electron Hall mobility for both 4H– and 6H–SiC polytypes is solely dominated by the anisotropy of the effective electron mass tensors.

In this article, we describe theoretical expressions of the electron Hall mobility and the Hall scattering factor, and then calculate the electron Hall mobility in nitrogen doped *n*-type 4H– and 6H–SiC as a function of temperature, net-doping concentration ($[N_D]$-$[N_A]$), and compensation ratio ($[N_A]/[N_D]$). The theoretically calculated electron mobility can be used as a standard measure for the evaluation of the crystalline perfection since structural defects such as points defects, dislocations, stacking faults, and micropipes lead to a further lowering of the mobility. If one compares the values of the experimentally obtained mobility with our theoretical calculation, one can qualitatively estimate the quality of the SiC sample. We also calculate the ratio of the Hall and drift mobility, i.e., the Hall scattering factor in 4H– and 6H–SiC, which is essential for the precise interpretation of Hall effect measurements. This work focuses on the Hall measurement configuration [$\mathbf{B}\|\mathbf{c}$, $\mathbf{j}\perp\mathbf{c}$] as shown in Fig. 1(a) since most of the Hall measurements on the device quality 4H– and 6H–SiC thin films are performed in this manner.

[a]Present address: Department of Physics and Measurement Technology, Linköping University, S-581 83 Linköping, Sweden; Electronic mail: hisaomi@ifm.liu.se
[b]Electronic mail: kitoh@appi.keio.ac.jp

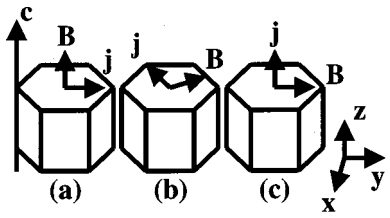

FIG. 1. Schematic diagram of the three distinct Hall measurement configurations: (a) [$\mathbf{B}\|\mathbf{c},\mathbf{j}\perp\mathbf{c}$], (b) [$\mathbf{B}\perp\mathbf{c},\mathbf{j}\perp\mathbf{c}$], and (c) [$\mathbf{B}\perp\mathbf{c},\mathbf{j}\|\mathbf{c}$] and the coordinate system we employed for a given sample.

TABLE I. Effective masses of 4H– and 6H–SiC.

	4H–SiC [m_0]	6H–SiC [m_0]
$m^*_{M\text{-}\Gamma}(m^*_1)$	0.57	0.75
$m^*_{M\text{-}K}(m^*_2)$	0.28	0.24
$m^*_{M\text{-}L}(m^*_3)$	0.31	1.83

II. METHOD AND MODEL

The purpose of this section is to provide explicit and easy to use analytical expressions of both the electron Hall mobility and the Hall scattering factor for the three distinct Hall measurement configurations as shown in Fig. 1. This section provides a summery of our model since the detailed procedure for the electron Hall mobility calculation has been described already in Ref. 11. It should be noted that we have performed further simplification of the model described in Ref. 11, which will be explained later in this section.

Our model is based on the conduction band structure determined recently by first-principles calculations and experiments.[14–20] We assume that there are six semiellipsoidal and parabolic constant energy surfaces centered exactly at M points in the first Brillouin zone for both 4H– and 6H–SiC, respectively. The effective masses along M-Γ, M-K, and M-L directions in the reciprocal space of the hexagonal unit cell are listed in Table I.[14] In order to obtain the conductivity tensor for a given SiC sample, we derive an expression of the conductivity tensor including the magnetic field for one ellipsoid from the Boltzmann transport equation using the relaxation time approximation and Maxwellian approximation. Then, we place three ellipsoids in proper positions in the reciprocal space by 120° rotation around the c axis, and add the contributions from each of the three ellipsoids. This procedure leads to the total conductivity tensor for a given SiC sample.

The electric current density vector $\mathbf{J}$ in the presence of the magnetic field $\mathbf{B}$ and the electric field $\mathbf{E}$ for a given SiC sample is described by the product of the conductivity tensor σ by $\mathbf{E}$:

$$\mathbf{J}=\sigma\mathbf{E}=\frac{3}{2}\begin{bmatrix}\sigma'_{11}+\sigma'_{22} & -(\sigma'_{12}+\sigma'_{21})B_z & (\sigma'_{13}+\sigma'_{23})B_y\\ (\sigma'_{12}+\sigma'_{21})B_z & \sigma'_{11}+\sigma'_{22} & -(\sigma'_{13}+\sigma'_{23})B_x\\ -(\sigma'_{31}+\sigma'_{32})B_y & (\sigma'_{31}+\sigma'_{32})B_x & 2\sigma'_{33}\end{bmatrix}\begin{bmatrix}E_x\\E_y\\E_z\end{bmatrix}, \tag{1}$$

where,

$$\sigma'_{ii}=qn'\frac{q}{m_i^*}\frac{\int_0^\infty \tau(x)x^{3/2}\exp(-x)dx}{\int_0^\infty x^{3/2}\exp(-x)dx}=qn'\frac{q}{m_i^*}\langle\tau\rangle, \tag{2a}$$

$$\sigma'_{ij}=qn'\frac{q^2}{m_i^*m_j^*}\frac{\int_0^\infty \tau^2(x)x^{3/2}\exp(-x)dx}{\int_0^\infty x^{3/2}\exp(-x)dx}$$

$$=qn'\frac{q^2}{m_i^*m_j^*}\langle\tau^2\rangle, \tag{2b}$$

and,

$$n'=2\left(\frac{m^*_{d.s.}k_BT}{2\pi\hbar^2}\right)^{3/2}\exp\{-(E_C-E_F)/k_BT\}, \tag{3}$$

$$m^*_{d.s.}=(m_1^*m_2^*m_3^*)^{1/3}, \tag{4}$$

$$x=\frac{\epsilon}{k_BT}. \tag{5}$$

q is the electron charge, k_B is the Boltzmann constant, T is the temperature, $m^*_{i,j=1,2,3}$ is the ith or jth component of the effective mass, and $\tau(x)$ is the electron momentum relaxation time for an electron having the kinetic energy ϵ, which is related to x by Eq. (5). The subscripts $i,j=1,2,3$ correspond to the directions for one ellipsoidal constant energy surface taken along the M-Γ, M-K, and M-L directions, respectively. The subscripts x,y,z correspond to the coordinate system shown in Fig. 1. n' is the electron concentration in each ellipsoid, where $m^*_{d.s.}$ is the density of states effective mass, E_C is the energy level of the conduction band minima, and E_F is Fermi level.

From this conductivity tensor, we can derive the mathematical expressions of the Hall coefficient, the electron Hall mobility, and the Hall scattering factor for the three distinct Hall measurement configurations as shown in Figs. 1(a) [$\mathbf{B}\|\mathbf{c}$, $\mathbf{j}\perp\mathbf{c}$], 1(b) [$\mathbf{B}\perp\mathbf{c}$, $\mathbf{j}\perp\mathbf{c}$], and 1(c) [$\mathbf{B}\perp\mathbf{c}$, $\mathbf{j}\|\mathbf{c}$]. The electron conductivity and the electron drift mobility, that are perpendicular and parallel to the c axis, respectively, are also derived.

The electron conductivity $\sigma_\perp$ and $\sigma_\|$, that are perpendicular and parallel to the c axis, respectively, are given by

$$\sigma_\perp=\frac{3}{2}(\sigma'_{11}+\sigma'_{22})=(3n')\frac{q}{2}\left(\frac{1}{m_1^*}+\frac{1}{m_2^*}\right)q\langle\tau\rangle, \tag{6a}$$

$$\sigma_{\parallel}=\frac{3}{2}(2\sigma'_{33})=(3n')q\frac{q\langle\tau\rangle}{m_3^*}. \tag{6b}$$

The electron drift mobility $\mu_{D(\perp)}$ and $\mu_{D(\parallel)}$, that are perpendicular and parallel to the c axis, respectively, are given by

$$\mu_{D(\perp)}=\frac{\sigma_{\perp}}{(3n')q}=\frac{1}{2}\left(\frac{1}{m_1^*}+\frac{1}{m_2^*}\right)q\langle\tau\rangle, \tag{7a}$$

$$\mu_{D(\parallel)}=\frac{\sigma_{\parallel}}{(3n')q}=\frac{q\langle\tau\rangle}{m_3^*}. \tag{7b}$$

The Hall coefficient $R_{H(a)}$, $R_{H(b)}$, and $R_{H(c)}$ for the three Hall measurement configurations shown in Figs. 1(a) [$\mathbf{B}\parallel\mathbf{c}$, $\mathbf{j}\perp\mathbf{c}$], 1(b) [$\mathbf{B}\perp\mathbf{c}$, $\mathbf{j}\perp\mathbf{c}$], and 1(c) [$\mathbf{B}\perp\mathbf{c}$, $\mathbf{j}\parallel\mathbf{c}$], respectively, are given by

$$R_{H(a)}=\frac{\frac{3}{2}(\sigma'_{12}+\sigma'_{21})}{(\frac{3}{2}(\sigma'_{11}+\sigma'_{22}))^2}=\frac{1}{(3n')q}\frac{4m_1^*m_2^*}{(m_1^*+m_2^*)^2}\frac{\langle\tau^2\rangle}{\langle\tau\rangle^2}, \tag{8a}$$

$$R_{H(b)}=\frac{\frac{3}{2}(\sigma'_{31}+\sigma'_{32})}{(\frac{3}{2}(\sigma'_{11}+\sigma'_{22}))(\frac{3}{2}\times 2\sigma'_{33})}=\frac{1}{(3n')q}\frac{\langle\tau^2\rangle}{\langle\tau\rangle^2}, \tag{8b}$$

$$R_{H(c)}=\frac{\frac{3}{2}(\sigma'_{13}+\sigma'_{23})}{(\frac{3}{2}(\sigma'_{11}+\sigma'_{22}))(\frac{3}{2}\times 2\sigma'_{33})}=\frac{1}{(3n')q}\frac{\langle\tau^2\rangle}{\langle\tau\rangle^2}. \tag{8c}$$

The electron Hall mobility $\mu_{H(a)}$, $\mu_{H(b)}$, and $\mu_{H(c)}$ for the three Hall measurement configurations shown in Figs. 1(a) [$\mathbf{B}\parallel\mathbf{c}$, $\mathbf{j}\perp\mathbf{c}$], 1(b) [$\mathbf{B}\perp\mathbf{c}$, $\mathbf{j}\perp\mathbf{c}$], and 1(c) [$\mathbf{B}\perp\mathbf{c}$, $\mathbf{j}\parallel\mathbf{c}$], respectively, are given by

$$\mu_{H(a)}=R_{H(a)}\sigma_{\perp}=q\frac{2}{m_1^*+m_2^*}\frac{\langle\tau^2\rangle}{\langle\tau\rangle}, \tag{9a}$$

$$\mu_{H(b)}=R_{H(b)}\sigma_{\perp}=\frac{q}{2}\left[\frac{1}{m_1^*}+\frac{1}{m_2^*}\right]\frac{\langle\tau^2\rangle}{\langle\tau\rangle}, \tag{9b}$$

$$\mu_{H(c)}=R_{H(c)}\sigma_{\parallel}=q\frac{1}{m_3^*}\frac{\langle\tau^2\rangle}{\langle\tau\rangle}. \tag{9c}$$

The Hall scattering factor $r_{H(a)}$, $r_{H(b)}$, and $r_{H(c)}$ for the three Hall measurements configurations shown in Figs. 1(a) [$\mathbf{B}\parallel\mathbf{c}$, $\mathbf{j}\perp\mathbf{c}$], 1(b) [$\mathbf{B}\perp\mathbf{c}$, $\mathbf{j}\perp\mathbf{c}$], and 1(c) [$\mathbf{B}\perp\mathbf{c}$, $\mathbf{j}\parallel\mathbf{c}$], respectively, are given by

$$r_{H(a)}=\frac{\mu_{H(a)}}{\mu_{D(\perp)}}=\frac{4m_1^*m_2^*}{(m_1^*+m_2^*)^2}\cdot\frac{\langle\tau^2\rangle}{\langle\tau\rangle^2}, \tag{10a}$$

$$r_{H(b)}=\frac{\mu_{H(b)}}{\mu_{D(\perp)}}=\frac{\langle\tau^2\rangle}{\langle\tau\rangle^2}, \tag{10b}$$

$$r_{H(c)}=\frac{\mu_{H(c)}}{\mu_{D(\parallel)}}=\frac{\langle\tau^2\rangle}{\langle\tau\rangle^2}. \tag{10c}$$

Equations (6)–(10) are functions of the effective masses and the average momentum relaxation time. Since the effective mass tensors have already been obtained by the recent first-principles calculations and the experiments,[14–20] we need to determine the values of $\langle\tau\rangle$ and $\langle\tau^2\rangle$ in order to calculate the electron Hall mobility and the Hall scattering factor. The following five scattering mechanisms are considered for the calculation of relaxation times: acoustic phonon deformation potential scattering, polar optical phonon scattering, intervalley phonon deformation potential scattering, neutral impurity scattering, and ionized impurity scattering.

The scattering rate for acoustic phonon deformation potential scattering τ_{ac}^{-1} is given by[21–23]

$$\tau_{ac}^{-1}(x)=\frac{\sqrt{2}(k_BTm_{d.s.}^*)^{2/3}D_{ac}^2}{\pi\hbar^4\rho v_s^2}x^{1/2}, \tag{11}$$

where D_{ac} is the acoustic deformation potential, ρ is the density, and v_s is the sound velocity in a particular semiconductor.

The scattering rate for polar optical phonon scattering τ_{pop}^{-1} is given by[21,22,24]

$$\begin{aligned}\tau_{pop}^{-1}(x)=&\frac{q^2\omega_p(\kappa_S/\kappa_\infty-1)}{4\pi\kappa_S\epsilon_0\hbar\sqrt{2xk_BT/m_{d.s.}^*}}\\&\times\Bigg[n(\omega_p)(1+\hbar\omega_p/xk_BT)^{1/2}\\&+\{n(\omega_p)+1\}\mathrm{Re}(1-\hbar\omega_p/xk_BT)^{1/2}\\&-\frac{\hbar\omega_pn(\omega_p)}{xk_BT}\sinh^{-1}(xk_BT/\hbar\omega_p)^{1/2}\\&+\frac{\hbar\omega_p\{n(\omega_p)+1\}}{xk_BT}\\&\times\sinh^{-1}[\mathrm{Re}(xk_BT/\hbar\omega_p-1)^{1/2}]\Bigg],\end{aligned} \tag{12}$$

where $n(\omega)=1/\{\exp(\hbar\omega/k_BT)-1\}$ is the Bose–Einstein distribution function, κ_S is the static relative dielectric constant in a semiconductor, κ_∞ is the optical relative dielectric constant in a semiconductor, ϵ_0 is the dielectric constant in vacuum, and $\hbar\omega_p$ is the polar optical phonon energy.

The scattering rate for intervalley phonon deformation potential scattering τ_{int}^{-1} is given by[21,22,25]

$$\begin{aligned}\tau_{int}^{-1}(x)=&\frac{ZD_{int}^2m_{d.s.}^{*3/2}}{\sqrt{2}\pi\hbar^3\omega_{int}\rho}[n(\omega_{int})(xk_BT+\hbar\omega_{int})^{1/2}\\&+\{n(\omega_{int})+1\}\mathrm{Re}(xk_BT-\hbar\omega_{int})^{1/2}],\end{aligned} \tag{13}$$

where $\hbar\omega_{int}$ is the energy of the intervalley phonon, D_{int} is the intervalley phonon deformation potential, and Z is the number of final equivalent valleys available for intervalley scattering. $Z=4$ is assumed for both 4H– and 6H–SiC.[11]

The scattering rate for neutral impurity scattering τ_{neu}^{-1} is given by[21,22,26]

$$\tau_{neu}^{-1}(x)=\frac{80\pi\kappa_S\epsilon_0n_{neu}(T)\hbar^3}{m_{d.s.}^{*\,2}q^2}, \tag{14}$$

where $n_{neu}(T)$ is the concentration of neutral impurities.

The scattering rate for ionized impurity scattering τ_{ion}^{-1} is given by[21,22,27]

$$\tau_{\text{ion}}^{-1}(x)=\frac{n_{\text{ion}}(T)q^4}{16\sqrt{2m_{d.s.}^*}\pi\kappa_S^2\epsilon_0^2}\left[\ln(1+\gamma^2)-\frac{\gamma^2}{1+\gamma^2}\right]\times(xk_BT)^{-3/2}, \tag{15}$$

where,

$$\gamma^2=8m_{d.s.}^*xk_BTL_D^2/\hbar^2, \tag{16}$$

$n_{\text{ion}}(T)$ is the concentration of ionized impurities and L_D is the screening length. The screening length is calculated using the standard Brooks and Herring model. The screening length L_D is given by

$$L_D=\left(\frac{\kappa_S\epsilon_0k_BT}{q^2}\right)^{1/2}\times\left(n(T)+\frac{(N_D-N_A-n(T))(N_A+n(T))}{N_D}\right)^{-1/2}. \tag{17}$$

In order to calculate the scattering rate for neutral and ionized impurity scattering we need to know the values of $n_{\text{neu}}(T)$ and $n_{\text{ion}}(T)$. For a nondegenerate *n*-type semiconductor with parabolic bands, the free electron concentration $n(T)$ is determined by the charge neutrality equation. The neutrality equation of the *n*-type 4H– and 6H–SiC is given by[28,29]

$$n(T)+N_A=\frac{N(h)}{1+(\text{gn}(T)/N_c)\exp[\Delta E(h)/k_BT]}+\frac{N(k)}{1+(\text{gn}(T)/N_c)\exp[\Delta E(k)/k_BT]}, \tag{18}$$

where,

$$N_C=2M_C\left(\frac{m_{d.s.}^*k_BT}{2\pi\hbar^2}\right)^{3/2} \tag{19}$$

is the effective density of states, N_A is the concentration of acceptors, N_D is the concentration of donors, M_C is the number of equivalent conduction band minima, $N(h)$ and $N(k)$ are the nitrogen concentrations in hexagonal and cubic lattice sites, respectively, $\Delta E(h)$ and $\Delta E(k)$ are the ionization energies of the nitrogen donor in hexagonal and cubic lattice sites, respectively, and *g* is the spin degeneracy factor. Based on the number of hexagonal and cubic sites, the concentration ratios $N(h)$ and $N(k)$ for 4H– and 6H–SiC are assumed to be 1:1 and 1:2, respectively. For both 4H– and 6H–SiC, $M_C=3$ and $g=2$ are employed. Table II lists the values of the ionization energies of the nitrogen donor in hexagonal and cubic lattice sites for 4H– and 6H–SiC.[30] The concentration of ionized impurities $n_{\text{ion}}(T)$ and neutral impurities $n_{\text{ion}}(T)$ are given by $n_{\text{ion}}(T)=2N_A+n(T)$ and $n_{\text{ion}}(T)=N_D-N_A-n(T)$, respectively.

TABLE II. Ionization energies of the nitrogen donor.

	4H–SiC (meV)	6H–SiO (meV)
$\Delta E(h)$	59	85
$\Delta E(k)$	102	125

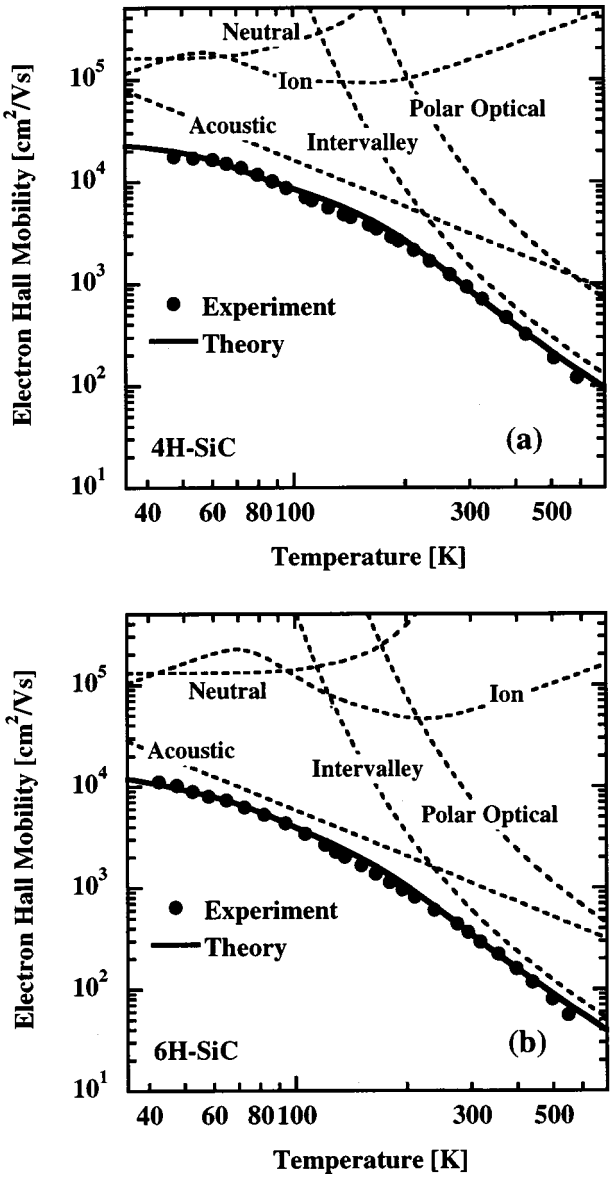

FIG. 2. Comparison of our Hall mobility calculations (solid curve) with the Hall effect measurements (filled circles) in the configuration [$\mathbf{j}\perp\mathbf{c},\mathbf{B}\|\mathbf{c}$] as shown in Fig. 1 (a) for (a) 4H–SiC and (b) 6H–SiC. The contribution of various scattering mechanisms to the total electron Hall mobility is also shown. Experimental data of 4H–SiC and 6H–SiC are taken from Ref. 30 and Ref. 33, respectively.

Combining the aforementioned five scattering mechanisms, we obtain the average momentum relaxation time by

TABLE III. Parameters used for the calculation of the relaxation time.

	4H–SiC	6H–SiC
Static relative dielectric constant κ_0	9.7	9.7
Optical relative dielectric constant κ_∞	6.5	6.5
Density ρ (g/cm^3)	3.166	3.166
Sound velocity v_s(10^4 m/s)	1.37	1.37
Acoustic deformation potential D_{ac} (eV)	11.6	11.2
Polor optical phonon energy $\hbar\omega_p$ (meV)	120	120
Intervalley deformation potential D_{int}(10^9 eV/cm)	2.3	2.1
Intervalley phonon energy $\hbar\omega_{\text{int}}$ (meV)	85	85

$$\langle \tau \rangle = \frac{\int_0^\infty \frac{x^{3/2}\exp(-x)dx}{\tau_{\rm neu}^{-1}(x)+\tau_{\rm ion}^{-1}(x)+\tau_{\rm ac}^{-1}(x)+\tau_{\rm pop}^{-1}(x)+\tau_{\rm int}^{-1}(x)}}{\int_0^\infty x^{3/2}\exp(-x)dx}, \tag{20a}$$

$$\langle \tau^2 \rangle = \frac{\int_0^\infty \frac{x^{3/2}\exp(-x)dx}{[\tau_{\rm neu}^{-1}(x)+\tau_{\rm ion}^{-1}(x)+\tau_{\rm ac}^{-1}(x)+\tau_{\rm pop}^{-1}(x)+\tau_{\rm int}^{-1}(x)]^2}}{\int_0^\infty x^{3/2}\exp(-x)dx}. \tag{20b}$$

The values of the parameters, κ_0, κ_∞, ρ, v_s, $D_{\rm ac}$, $\hbar\omega_p$, $D_{\rm int}$, and $\hbar\omega_{\rm int}$, are listed in Table III. Since large discrepancies arise in literature concerning the values of the acoustic deformation potential $D_{\rm ac}$ and very little is known about the scattering mechanisms in high temperature region for *n*-type 4H– and 6H–SiC,[3–11] our theoretical approach has two adjustable parameters, $D_{\rm ac}$ and $D_{\rm int}$. Our knowledge of the deformation potential constants is the least perfect compared to that of all the other parameters involved in the expressions for the transport coefficient. If there is a temperature region in which the acoustic phonon scattering predominate, one can deduce the acoustic deformation potential constant $D_{\rm ac}$ from the value of the mobility in that temperature region.[31] The applicability of the assumption of relatively pure acoustic phonon scattering may be judged from the temperature dependence of mobility, which should be proportional to $T^{-3/2}$. The $T^{-3/2}$ temperature dependences of mobility have been observed very clearly for both 4H– and 6H–SiC in Figs. 2(a) and 2(b), that we believe the acoustic deformation potentials which we obtained from the fitting procedure are very close to the intrinsic ones. On the other hand, the observed temperature dependence of mobility above $T=200\,$K for both 4H– and 6H–SiC cannot be explained by acoustic phonon scattering only. We assume that the polar optical phonon scattering and intervalley phonon deformation potential scattering dominate the mobility in that temperature region. However, it is difficult to make a unique fit when intervalley scattering is important since the electron may be scattered by more than one type of phonons, and each phonon has a different deformation potential constant.[25,31,32] The complicated phonon dispersions of 4H– and 6H–SiC make this fitting procedure enormously difficult. For example, since 6H–SiC has 12 atoms per unit cell, i.e., there could be as many as 36 phonon branches in its E-k dispersion. Therefore, we employ a simplification for intervalley scattering. The effect of all intervalley scattering is represented by only one phonon having the energy of 85 meV.[6,11] The intervalley deformation potential constants $D_{\rm int}$ for 4H– and 6H–SiC are obtained by a numerical fitting of the experimentally obtained mobility data. In the aforementioned fitting procedure of $D_{\rm ac}$ and $D_{\rm int}$, we should employ the samples with high crystalline quality since crystal defects such as points defects, dislocations, stacking faults, and micropipes lead to a further lowering of the mobility and it is, in practice, difficult to calculate the quantitative effect of these defects.

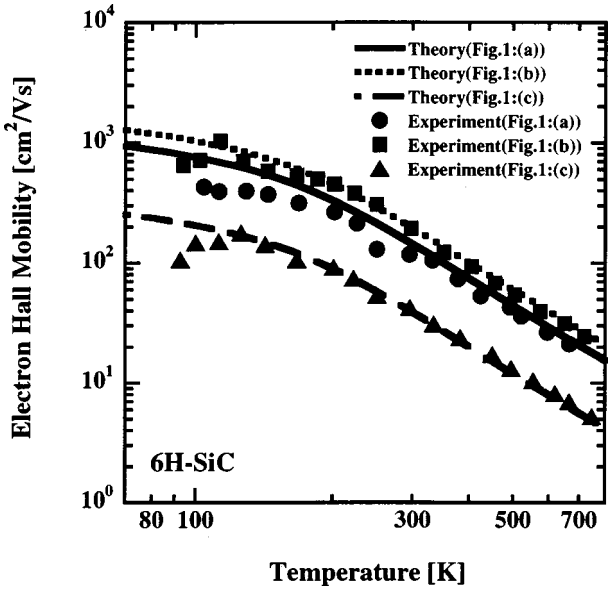

FIG. 3. Electron Hall mobility for the three distinct Hall measurement configurations as shown in Fig. 1. Experimental data are taken from Ref. 11. We calculated these mobilities using the same model described in this article with the calculation parameters used in Ref. 11. Since this bulk crystal is expected to contain many crystal defects such as dislocations, we cannot calculate the mobility with the same calculation parameters presented in this work. The detailed description on these problems has been given in Ref. 11.

In this work, we assume that the momentum relaxation time can be described as a function of the kinetic energy of the electron, not the wave number vector, i.e., the only anisotropy of the electron effective mass tensors determines the anisotropy of the transport phenomena in 4H– and 6H–SiC. Although it is difficult to justify this assumption, this enables us to derive far more explicit and simple expressions to describe transport phenomena in 4H– and 6H–SiC. Figure 3 shows the anisotropy of the electron Hall mobility in 6H–SiC, in which our model precisely reproduces the relative change in the electron Hall mobility for the three Hall measurements configurations as shown in Figs. 1(a) [$\mathbf{B}\|\mathbf{c}$, $\mathbf{j}\perp\mathbf{c}$], 1(b) [$\mathbf{B}\perp\mathbf{c}$, $\mathbf{j}\perp\mathbf{c}$], and 1(c) [$\mathbf{B}\perp\mathbf{c}$, $\mathbf{j}\|\mathbf{c}$]. Our model reproduces the anisotropy of the electron Hall mobility in 4H–SiC as well. This good agreement with the experimental results probably justifies our assumption.

III. RESULTS AND DISCUSSIONS

Figure 2 shows the comparison of our Hall mobility calculations with the Hall effect measurements in the configuration [$\mathbf{j}\perp\mathbf{c}$, $\mathbf{B}\|\mathbf{c}$] as shown in Fig. 1(a) for (a) 4H– and (b) 6H–SiC. The 4H–SiC sample is an epitaxially grown thin film having $N_D=3.0\times10^{15}\,{\rm cm}^{-3}$ and $N_A=1.0\times10^{14}\,{\rm cm}^{-3}$.[14] The 6H–SiC sample is also an epitaxially grown thin film having $N_D=1.05\times10^{16}\,{\rm cm}^{-3}$ and $N_A=1.0\times10^{14}\,{\rm cm}^{-3}$.[33] Our calculations for both 4H–SiC and 6H–SiC agree very well with the experiments. In the low temperature region ($T<70\,$K), ionized impurity scattering and neutral impurity scattering become important. The agreement with the experiments for both 4H– and 6H–SiC in this temperature region is remarkable, since these two scattering mechanisms have no adjustable parameters. This confirms the accuracy of our model. In our calculation, the most dominant scattering

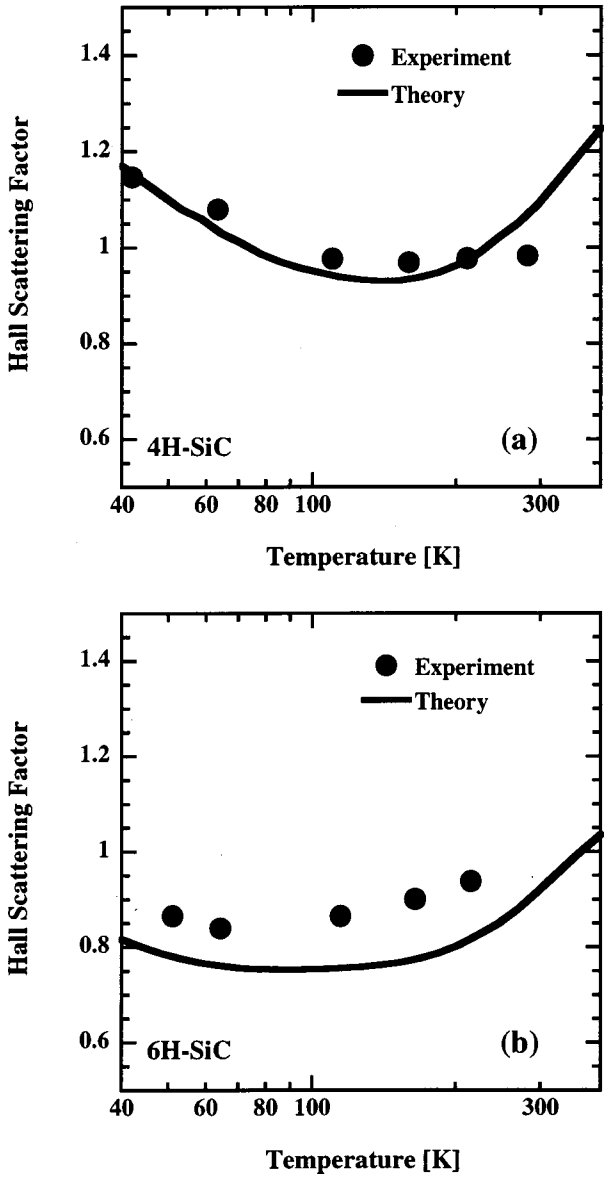

FIG. 4. Comparison of our Hall scattering factor calculations (solid curve) with the experimental results (filled circles) in the configuration [$\mathbf{j}\perp\mathbf{c}$, $\mathbf{B}\|\mathbf{c}$] as shown in Fig. 1(a) for (a) 4H–SiC and (b) 6H–SiC. Experimental date of 4H–SiC and 6H–SiC are taken from Ref. 34.

mechanism for both 4H– and 6H–SiC changes from acoustic phonon scattering to intervalley scattering at the temperature between 200 and 300 K. The change of slope at this temperature can be seen in the experimental data as well. Notice that the calculation parameters for both 4H– and 6H–SiC listed in Table III are almost identical. This coincidence implies that the characteristic and totally different transport properties of 4H– and 6H–SiC are solely dominated by their effective electron mass tensors.

Figure 4 shows the comparison of our Hall scattering factor calculations with the Hall effect measurements in the configuration [$\mathbf{j}\perp\mathbf{c}$, $\mathbf{B}\|\mathbf{c}$] as shown in Fig. 1(a) for (a) 4H– and (b) 6H–SiC. The 4H–SiC sample is an epitaxially grown thin film having $N_D=7.0\times10^{15}\,\mathrm{cm}^{-3}$ and $N_A=1.3\times10^{15}\,\mathrm{cm}^{-3}$.[33,34] The 6H–SiC sample is also an epitaxially grown thin film having $N_D=9.0\times10^{15}\,\mathrm{cm}^{-3}$ and $N_A=5.6\times10^{14}\,\mathrm{cm}^{-3}$.[34] For 4H–SiC our calculation, which is essentially the same as the one reported in Ref. 13, agrees very well with the experiments. As to 6H–SiC, our calculation reproduces qualitative feature of experimental data very well. These good agreements with the experimental results indicate that we have constructed a proper scattering model for 4H– and 6H–SiC. The small deviation of the absolute values between our theory and the experiment for 6H–SiC is likely due to the anisotropic scattering mechanisms which we neglect in this work. The stronger anisotropy of the electron effective mass tensor in 6H–SiC, compared to 4H–SiC, may break slightly our assumption that the scattering mechanisms in SiC are isotropic.

Figure 5 shows the electron Hall mobility as a function of the net-doping concentration ($[N_D]$-$[N_A]$) and the compensation ratio ($[N_A]/[N_D]$) at 77 and 300 K with the Hall measurement configuration [$\mathbf{j}\perp\mathbf{c}$, $\mathbf{B}\|\mathbf{c}$] as shown in Fig. 1(a). The electron Hall mobility depends strongly on the compensation ratio. At $T=77$ K, the difference between the curves, compensation ratio$=0$ and 0.1, is large for both 4H– and 6H–SiC [Figs. 5(a) and 5(c)] because ionized impurity scattering by compensated donors and compensating acceptors dominates the total mobility. This difference for 6H–SiC is larger than for 4H–SiC because the ionization energy of the nitrogen donors in 6H–SiC is larger than in 4H–SiC. At this temperature, most of the nitrogen donors in 6H–SiC are frozen out, while some of the nitrogen donors in 4H–SiC are still ionized, therefore, if the sample is not compensated at all, the only neutral impurity scattering dominates the mobility of 6H–SiC, while the ionized impurity scattering still contributes to the mobility of 4H–SiC. In Figs. 5(b) and 5(d), the electron Hall mobility of different compensation ratios converge to a constant value when the net-doping concentration becomes smaller than $10^{14}\,\mathrm{cm}^{-3}$ because the contribution of the ionized impurity scattering and the neutral impurity scattering to the total mobility becomes negligibly small. We believe Figs. 5 (a)–5(d) serve as a standard measure for the crystalline perfection of SiC samples, and are useful for crystal growers who want to characterize the quality of SiC they grow. Using Figs. 5(a)–5(d) one can determine the compensation ratio of a given sample from the experimentally measured mobility data if the quality of the sample is good enough. These date are also essential to perform reliable device simulations.

IV. CONCLUSION

We have performed the theoretical calculation of the electron Hall mobility in nitrogen doped *n*-type 4H– and 6H–SiC as a function of temperature, net-doping concentration ($[N_D]$-$[N_A]$), and compensation ratio ($[N_A]/[N_D]$).[35–37] The electron Hall mobility has been calculated for two temperatures, $T=77$ and 300 K, covering a wide range of the net-doping concentration [10^{14}–$10^{18}(\mathrm{cm}^{-3})$] and the compensation ratio (0–0.6). The contribution of various scattering mechanisms to the total electron Hall mobility has been found for both 4H– and

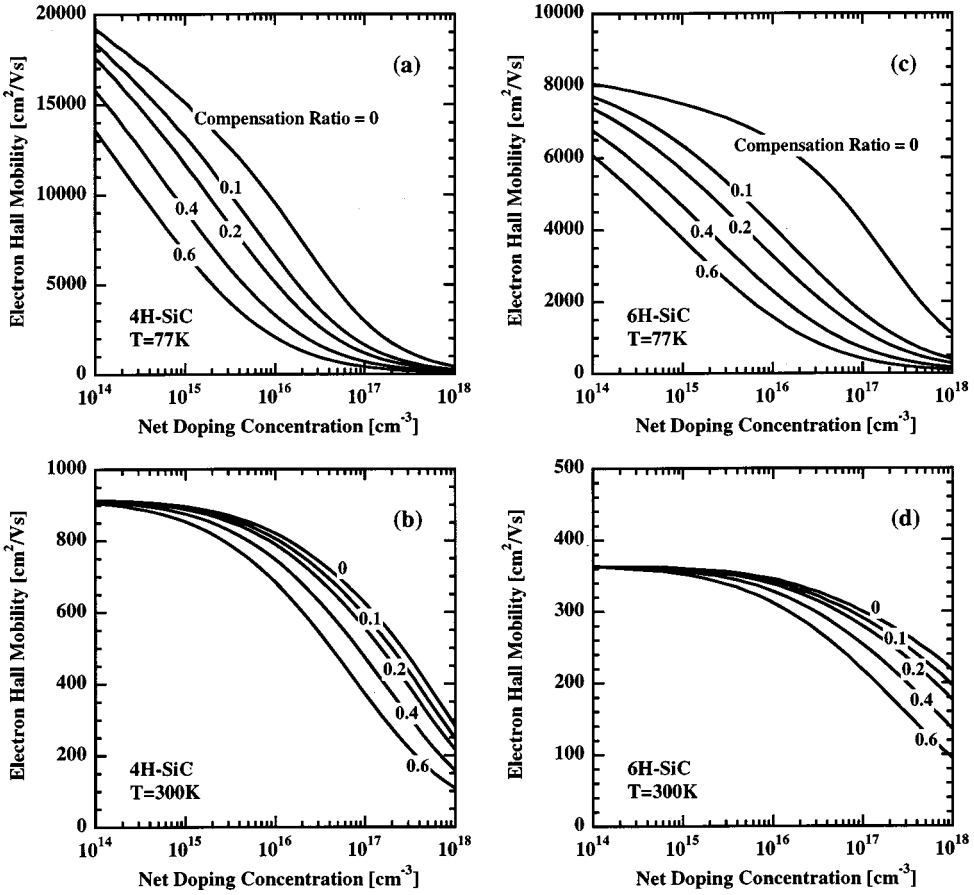

FIG. 5. Electron Hall mobility in the configuration [$\mathbf{j}\perp\mathbf{c},\mathbf{B}\|\mathbf{c}$] as shown in Fig. 1 (a) as a function of the net-doping concentration ($[N_D]$-$[N_A]$) and compensation ratio ($[N_A]/[N_D]$) for (a) 4H–SiC at $T=77$ K, (b) 4H–SiC at $T=300$ K, (c) 6H–SiC at $T=77$ K, and (d) 6H–SiC at $T=300$ K.

6H–SiC. The Hall scattering factor in 4H– and 6H–SiC has been calculated. These calculations are in good agreement with experimental results.

ACKNOWLEDGMENTS

The authors thank T. Kinoshita, T. Yokogawa, G. Pensl, M. Schadt, W. J. Choyke, R. P. Devaty, H. -E. Nilsson, and E. Bellotti for fruitful discussions.

[1] K. Shenai, R. S. Scott, and B. J. Baliga, IEEE Trans. Electron Devices **36**, 1811 (1989).
[2] T. P. Chow and R. Tyagi, IEEE Trans. Electron Devices **41**, 1481 (1994).
[3] R. P. Joshi, J. Appl. Phys. **78**, 5518 (1995).
[4] R. P. Joshi and D. K. Ferry, Solid-State Electron. **38**, 1911 (1995).
[5] H.-E. Nilsson, U. Sannemo, and C. S. Petersson, J. Appl. Phys. **80**, 3365 (1996).
[6] R. Mickevičius and J. H. Zhao, J. Appl. Phys. **83**, 3161 (1998).
[7] H.-E. Nilsson, M. Hjelm, and C. Fröjdh, J. Appl. Phys. **86**, 965 (1999).
[8] T. Kinoshita, K. M. Itoh, J. Muto, M. Schadt, G. Pensl, and K. Takeda, Mater. Sci. Forum **264**, 295 (1998).
[9] T. Kinoshita, K. M. Itoh, M. Schadt, and G. Pensl, J. Appl. Phys. **85**, 8193 (1999).
[10] H. Iwata and K. M. Itoh, Mater. Sci. Forum **338**, 729 (2000).
[11] H. Iwata, K. M. Itoh, and G. Pensl, J. Appl. Phys. **88**, 1956 (2000).
[12] M. Schadt, G. Pensl, R. P. Devaty, W. J. Choyke, R. Stein, and D. Stephani, Appl. Phys. Lett. **65**, 312 (1994).
[13] G. Rutsch, R. P. Devaty, W. J. Choyke, D. W. Langer, L. B. Rowland, E. Niemann, and F. Wischmeyer, Mater. Sci. Forum **338**, 733 (2000).
[14] C. Persson and U. Lindefelt, Phys. Rev. B **54**, 10257 (1996); J. Appl. Phys. **82**, 5496 (1997).
[15] W. R. L. Lambrecht and B. Segall, Phys. Rev. B **54**, R2249 (1995).
[16] N. T. Son, O. Kordina, A. O. Konstantinov, W. M. Chen, E. Sörman, B. Monemar, and E. Janzén, Appl. Phys. Lett. **65**, 3209 (1994).
[17] N. T. Son, W. M. Chen, O. Kordina, A. O. Konstantinov, B. Monemar, E. Janzén, D. M. Hofman, D. Volm, M. Drechsler, and B. K. Meyer, Appl. Phys. Lett. **66**, 1074 (1994).
[18] G. Wellenhofer and U. Rössler, Phys. Status Solidi B **202**, 107 (1997).
[19] W. R. L. Lambrecht, S. Limpijumnong, S. N. Rashkeev, and B. Segall, Phys. Status Solidi B **202**, 5 (1997).
[20] B. K. Meyer, D. M. Hofmann, D. Volm, W. M. Chen, N. T. Son, and E. Janzén, Phys. Rev. B **61**, 4844 (2000).
[21] M. Lundstorm, *Fundamentals of Carrier Transport*, Modular Series on Solid State Devices, Vol. X (Addison–Wesley, Reading, MA, 1990).
[22] B. K. Ridley, *Quantum Processes in Semiconductors*, 3rd. ed. (Clarendon, Oxford, 1992).
[23] J. Bardeen and W. Shockley, Phys. Rev. **80**, 72 (1950).
[24] H. Callen, Phys. Rev. **76**, 1394 (1949).
[25] D. K. Ferry, Phys. Rev. B **14**, 1605 (1976).
[26] C. Erginsoy, Phys. Rev. **131**, 79 (1950).
[27] H. Brooks, Phys. Rev. **83**, 879 (1951).
[28] W. Suttrop, G. Pensl, W. J. Choyke, R. Stein, and S. Leibenzeder, J. Appl. Phys. **72**, 3708 (1992).
[29] W. Götz, A. Schöner, G. Pensl, W. Suttrop, W. J. Choyke, R. Stein, and S. Leibenzeder, J. Appl. Phys. **73**, 3332 (1993).
[30] W. J. Choyke and G. Pensl, MRS Bull. **22**, 25 (1997).
[31] D. Long, Phys. Rev. **120**, 2024 (1960).
[32] G. Weinreich, T. M. Sanders, and H. G. White, Phys. Rev. **114**, 33 (1959).
[33] S. Karmann, W. Suttrop, A. Schöner, M. Schadt, C. Haberstroh, F. Engelbrecht, R. Helbig, and G. Pensl, J. Appl. Phys. **72**, 5437 (1992).
[34] G. Rutsch, R. P. Devaty, W. J. Choyke, D. W. Langer, and L. B. Rowland, J. Appl. Phys. **84**, 2062 (1998).
[35] J. Pernot, S. Contreras, J. Camassel, J. L. Robert, W. Zawadzki, E. Neyret, and L. D. Cioccio, Appl. Phys. Lett. **77**, 4359 (2000).
[36] S. Dhar and S. Ghosh, J. Appl. Phys. **88**, 6519 (2000).
[37] Recently, experimental data of the electron Hall mobility in 4H–SiC which correspond to our theoretical calculation of Fig. 5(b) have been provided.[35] They are in very good agreement with our calculation. A theoretical study on the low field electron mobility in 6H–SiC using iterative technique has also been published.[36]